

Metallic chemical potentials in an insulating topological state

Erica Kotta

New York University <https://orcid.org/0000-0003-3570-6161>

Yishuai Xu

New York University

Jaewoong Lee

Gwangju Institute of Science and Technology (GIST)

Shouzheng Liu

New York University <https://orcid.org/0000-0002-3389-5037>

Lin Miao

Southeast University <https://orcid.org/0000-0001-6236-6356>

Yi Xu

New York University

Denglin Jiang

New York University

Jonathan Denlinger

Lawrence Berkeley National Lab <https://orcid.org/0000-0001-7645-1631>

Turgut Yilmaz

Brookhaven National Laboratory <https://orcid.org/0000-0001-7571-0937>

Elio Vescovo

Brookhaven National Lab

Beongki Cho

Gwangju Institute of Science and Technology (GIST)

L. Andrew Wray (✉ lawray@nyu.edu)

New York University <https://orcid.org/0000-0001-8977-0201>

Article

Keywords:

Posted Date: February 22nd, 2022

DOI: <https://doi.org/10.21203/rs.3.rs-1239795/v1>

License:  This work is licensed under a Creative Commons Attribution 4.0 International License.

[Read Full License](#)

Metallic chemical potentials in an insulating topological state

Erica Kotta¹, Yishuai Xu¹, J. W. Lee², Shouzheng Liu¹, Lin Miao³, Yi Xu⁴, Denglin Jiang⁴,
Jonathan D. Denlinger⁵, Turgut Yilmaz⁶, Elio Vescovo⁶, B. K. Cho^{2,*}, and L. Andrew Wray^{1,*}

¹ Department of Physics, New York University, New York, New York 10003, USA

² School of Materials Science and Engineering, Gwangju Institute of Science and Technology
(GIST), Gwangju 61005, Korea

³ School of Physics, Southeast University, Nanjing, 211189, China

⁴ Center for Data Science (CDS), New York University, New York, New York 10011, USA

⁵ Advanced Light Source, Lawrence Berkeley National Laboratory, Berkeley, CA 94720, USA

⁶ National Synchrotron Light Source II, Brookhaven National Lab, Upton, New York 11973,
USA

* Corresponding author. Email: chobk@gist.ac.kr (B.K.C.); lawray@nyu.edu (L.A.W.)

Controlling the density of electrons inside an insulator via the chemical potential is a cornerstone of modern electronics, enabling the electrical conductivity of semiconductors and the emergence of fascinating new properties linked with electronic correlations. The compound SmB_6 has drawn widespread attention in recent years as the first insulator to feature both strong electronic correlations and topological quantum order¹⁻⁷, potentially enabling a host of new phenomenologies as charge density is modified. However, chemical potential has not been experimentally controlled in studies to date of the electronic structure. Here we present an angle-resolved photoemission spectromicroscopy (μ -ARPES) study of SmB_6 alloys, using the natural inhomogeneity of sample surfaces to create the analogue of a multi-dimensional doping series. The role of electronic correlations is observed in the interplay of the topologically ordered conducting states with one another and with the chemical potential. Higher doping is found to result in the transformation of these interdependencies as the disorder from impurities erodes quantum coherence. These findings set the stage for a holistic understanding of the interplay between strong correlations and topological features in the electron system. Moreover, they validate recent analyses suggesting that the electronic structure of SmB_6 can present the key hallmarks of conventional electron doping, such as a Fermi surface, while nonetheless preserving long-range insulating character in electrical transport measurements⁸⁻¹⁰.

The compound SmB_6 was identified over 50 years ago as the first known Kondo insulator¹¹, in which hybridization between strongly correlated $\text{Sm } 4f$ electrons and itinerant $\text{Sm } 5d$ states opens an insulating band gap at $T \sim < 35\text{K}$ ¹²⁻¹³. The material has been subject to further intense interest over the last few years, following the discovery that the $\text{Sm } 5d$ band creates a topological symmetry inversion at the reciprocal k space X-point, a scenario termed a topological Kondo insulator (TKI)¹⁴⁻¹⁵. Numerous ARPES studies have since observed topologically consistent in-gap surface states (SS, yellow curves in Fig. 1d) and spin texture of SmB_6 , corroborating the TKI picture^{2,4,6-7,16-18}. However, the charge density dependence of the electronic structure has been notoriously challenging to uncover due to the inhomogeneously polar surface termination, presenting a key obstacle to understanding the role of strong correlations in the material.

Here, we employ μ -ARPES to uncover the dependence of the SmB_6 electronic structure on the chemical potential and surface termination by mapping inhomogeneity within individual samples¹⁹. Sets of 576 individual ARPES images, measured across a 24×24 grid of points spaced $10 \mu\text{m}$ apart in the sample x-y plane, are taken along the M-X-M axis of the surface Brillouin Zone (Fig. 1b,d) for alloys $\text{Sm}_{0.95}\text{Eu}_{0.05}\text{B}_6$ and $\text{Sm}_{0.7}\text{Ce}_{0.3}\text{B}_6$ (termed “Eu05” and “Ce30,” respectively). Extensive characterization work done previously on these alloys shows that they both preserve the topological SS of SmB_6 and are nominally hole and electron doped, respectively²⁰⁻²¹. The Eu05 alloy is insulating at low temperature and extremely similar to undoped SmB_6 , featuring a roughly identical temperature dependence of the topological electronic structure²⁰, and a closely comparable bulk chemical potential distribution. It is favored over the undoped compound for this investigation due to presenting a superior cleaved surface for resolving spectral features (see Fig. S1 of **Extended Data and Figures**). Spatially averaged spectra in Fig. 1a show that the flat $4f$ bands are much broader in heavily alloyed Ce30, and the dispersive $5d$ band is $>100 \text{ meV}$ lower in energy, consistent with the nominal carrier doping.

Mapping Electronic Structure Inhomogeneity

The individual single-point ARPES images have limited statistics but allow clear characterization of key electronic structure properties such as the binding energy (E_{4f}) and width (Σ_i) of the ${}^6\text{H}_{5/2}$ $4f$ band feature at the momentum space X-point (see Fig. 1b and Methods). Other tracked features include the intensity of the $E = -0.7 \text{ eV}$ Sm^{2+} multiplet feature, correlating with

surface Sm density²²⁻²³, and the $k_x=0$ high-symmetry axis, which reveals the geometrical tilt angle of the surface.

The variation of these features across each sample surface is presented in Fig. 2. Histograms of the catalogued surfaces (Fig. 2e-h) show that the $4f$ spectral feature is both narrower by $\Delta\Sigma_i \sim 30$ meV and found $\Delta E_{4f} \sim 25$ meV closer to the Fermi level for the Eu05 sample. Maps of E_{4f} (Fig. 2d,l (right)) are taken to represent the position of the chemical potential within the $4f$ band structure, and reveal relatively smooth gradients across the surface of each sample, with a dynamic range of ~ 15 meV. Though striking to observe in an insulator, these gradients are consistent with typical bulk stoichiometric variations at the percent level in SmB_6 synthesis^{8,27,33-37} (see Methods).

In contrast to the smooth chemical potential gradients, the surface tilt maps show more varied regional fluctuations (Fig. 2a,i), and the termination chemistry (I_{Sm}) map of Eu05 shows terminal Sm density changing on a length scale of ~ 50 μm . Vertical stripe-like features, visible in all the feature maps, are an effect of mechanical hysteresis in the scan trajectory (see Methods). A clear imprint of I_{Sm} appears in the Eu05 width (Σ_i) map, however no imprint is seen on the E_{4f} map in spite of minimal fitting error ($dE_{4f} < 1$ meV). The $4f$ energy width is ~ 5 meV broader in regions with significant excess Sm, consistent with theoretical proposals that the Sm termination may contribute to Kondo state decoherence²⁷.

Compared with Eu05, the Ce30 feature maps (Fig. 2i-l) show very different correlations between mapped quantities. Strikingly, the surface termination (I_{Sm}) map is essentially devoid of features, with the majority of the surface resembling the Sm-poor regions of Eu05. No determinative correlation is visible between I_{Sm} and Σ_i or E_{4f} for Ce30, consistent with the lack of dynamic range in I_{Sm} . However, most features of the Ce30 Σ_i map are visibly anti-correlated with E_{4f} . This phenomenology suggests an interplay between f -electron imaginary self energy and the chemical potential, which is corroborated in our numerical modeling below.

Interplay of Bulk States with Charge Density

The interdependence of the $5d$ and $4f$ band energies (E_{5d} and E_{4f}) provides a basis to interpret the strongly correlated bulk physics and is evaluated for both samples in Fig. 3. Examining Eu05 ARPES images binned from surface regions with the highest and lowest $4f$ band energies reveals that the $5d$ band shifts in the same direction as the $4f$ band, and on a much larger ~ 0.1 eV scale (Fig. 3a). Tracked fits of E_{5d} (see Methods) summarized in Fig. 3d show that the $5d$ band spans a dynamic range of roughly ~ 150 meV in Eu05, but only ~ 20 meV in Ce30 where it is more than 100 meV deeper in binding energy. These properties of the $5d$ electron pocket can also be seen without fitting from constant-energy ARPES curves (Fig. 3c). In contrast, to the $5d$ band, the $4f$ state energy E_{4f} has a much smaller ~ 35 meV dynamic range across the two samples. In each sample it spans a ~ 10 meV range, centered near -40 meV in Ce30 and -15 meV in Eu05. Measurements on undoped SmB_6 show a mean value of $E_{4f} = -16$ eV with a slightly smaller dynamic range (see Extended Data Fig. S1), consistent with the expectation that Ce30 is electron doped and Eu05 is slightly hole doped.

A steady linear trend of the $5d$ energies can be seen in the more electron-doped regime of the $4f$ energies of the Eu05 data (Fig. 3d) with a mean slope $m_{df} = \Delta E_{5d} / \Delta E_{4f}$ of 15. This is a profound deviation from the $m_{df} = 1$ trend expected in a rigid shift picture (see $U=0$ curve in Fig. 3d). Values of $m_{df} \gg 1$ are a direct indicator of strong correlations and can be reproduced by adding a mean field Hubbard U term with a typical amplitude ($U=1$ eV, gray curve) to the $4f$ orbitals of the renormalized tight binding model from Ref. [20] (see Methods). The mechanism behind this is depicted in the Fig. 3e cartoon. As electrons are doped into the system, strong correlations cause the energy of the $4f$ states to rise significantly, and the chemical potential moves upward in tandem to conserve electron number. The net result is that the chemical potential appears to move up only slightly relative to the $4f$ states, and a far greater amount relative to the weakly correlated $5d$ band.

A very different behavior is expected when the chemical potential enters the bulk band gap, where shifts in the chemical potential incur negligible changes in the charge density, and thus a rigid shift ($m_{df} = 1$) picture is expected in the limit of a cleanly gapped spectrum. This is reflected in the simulated Eu05 data (Fig. 3d), where the steep slope (m_{df}) tapers off near $E_{4f} \sim -13$ meV, labeled ' E_C ' throughout Fig. 3-4. A sharp step in the histogram of E_{4f} values is also seen at E_{4f}

$\sim E_C$ (Fig. 3b). Assuming a uniform underlying distribution of electron- and hole-donating defects, such a step indicates a sudden drop in the electronic density of states (DOS) at the Fermi level, suggesting that the chemical potential μ sits at the edge of a state continuum when $E_{4f}=E_C$. As the material is an insulator, the relevant DOS continuum is likely to be associated with states derived from the conduction band, which may feature Anderson localization and/or an impurity band (see Fig. 4d diagram, based on theory in Ref. [25]). The observation that local regions appear to be doped into a band-like continuum is consistent with the interpretation of recent electron spin resonance measurements¹⁰ and provides a possible explanation for a remnant Fermi surface attributed from dHvA on insulating SmB₆ samples⁹.

In stark contrast to the Eu05 dataset, the dramatically reduced range of the $5d$ band energy in Ce30 *does* roughly correspond to expectations for a rigid shift doping picture, with a small slope of $m_{df} \sim 2.1 \pm 0.8$ (Fig. 3d). A partial explanation for this behavior may be found in the Fig. 2 feature maps, which show a strong correlation between $4f$ energy and $4f$ width across the Ce30 sample surface. This resembles a trend noted in earlier ARPES and dynamical mean field theory (DMFT) studies which found that $4f$ binding energy increases at roughly 1/4th the rate of the $4f$ width at half maximum, as temperature is increased above $\sim 20\text{K}$ ^{16,26}. This is also reproduced in numerical modeling of state energies when $4f$ width is taken to represent imaginary self energy (see Fig. 3d and Methods), which yields a slope of $m_{df} \sim 0.5$. The model behavior follows from charge conservation: when $4f$ states are shifted above the Fermi level due to broadening (decoherence), the chemical potential must move up to preserve electron number, leading to the appearance that the $4f$ and $5d$ bands have shifted down in energy. Large $4f$ self energy also directly reduces m_{df} (see Methods), and the observed trend likely stems from a convolution of these factors.

Variability of the Topological Surface State

To investigate the SS, Eu05 spectra are binned in a grid partitioned by the $4f$ energy E_{4f} and the surface termination I_{Sm} (Fig. 4a), analogous to a two-dimensional doping series. The horizontal axis of Fig. 4a represents the charge doping dependence of SmB₆, measured at Sm-poor (top row) or Sm-rich (bottom row) surface regions. The larger $4f$ feature energy width in Sm-rich regions contributes a greater background at the Fermi level, resulting in the growth of spectral

intensity at the extrapolated $5d$ band Fermi momentum ($k_x \sim 0.5 \text{ \AA}^{-1}$, see white curves). Data from Ce30 are not considered in this analysis, as the larger feature widths and consequent background are unsuitable for close quantitative analysis (see Methods).

Tracking the Eu05 SS Fermi momentum ($k_{F,SS}$, Fig. 4b) reveals a linear dependence on chemical potential for most of the data set, with a divergence between the Sm-rich and Sm-poor terminations for hole-doped regions ($E_{4f} > E_C$). The roughly identical SS energetics across surface terminations in most of the data ($E_{4f} < E_C$ in Fig. 4b) suggests that the observed energetic variation within this regime is driven by the bulk carrier doping. If we further assume a rigid shift picture, where all band energies shift in lock-step with each other, the dependence of SS k_F on E_{4f} can be used to estimate an $\overline{X-M}$ axis SS Fermi velocity of $v_{X-M} \sim 0.26$. However directly fitting the SS in the clearest panels of Fig. 4a (top row) reveals that the real velocity is twice as large ($v_{X-M} = 0.50 \text{ eV-\AA}$; see Methods Figure S5), suggesting that a rigid shift picture is grossly inadequate to explain the observed SS behavior.

This can be understood from the strongly correlated bulk physics identified in Fig. 3. Lowering the value of E_{5d} relative to E_{4f} enlarges the topological symmetry inversion region of momentum space, which in turn increases the SS Fermi momentum. Plugging the observed relative motion of E_{5d} and E_{4f} ($m_{diff} = 15$) into the tight binding model yields a $\Delta k_{F,SS} = 0.010 \text{ \AA}^{-1}$ correction to the motion of the SS Fermi momentum in the linear region of Fig. 4b (see Methods). This is roughly identical to the value of $\Delta k_{F,SS} = 0.009 \text{ \AA}^{-1}$ needed to explain the discrepancy between the observed SS Fermi velocity and the velocity attributed from doping dependence of the SS Fermi momentum.

At the hole-doped extreme of the data ($E_{4f} > E_C$ in Fig. 4b), the SS Fermi momentum of low- and medium- I_{Sm} surfaces shifts more slowly, approaching the rigid shift picture that is expected when the chemical potential enters a band gap. The SS Fermi momentum from Sm-richest regions undergoes a trend reversal, going back up to larger values at the most hole-doped data point. This may be due to the loss of bulk screening of a positive surface charge expected at the outermost layer of the polar Sm-terminated surface³⁸. The onset of these termination-dependent trends at the hole-doped end of the binning series suggests that bulk screening of the surface potential may

be significantly weaker in this region, consistent with the picture of the chemical potential at $E_{4f}=E_C$ being located at the edge of the conduction band or closely associated DOS continuum (Fig. 4d).

Discussion

It is a foundational principle of quantum materials research that the interplay of chemical potential with strong local electronic interactions often leads to the emergence of remarkable physical properties. For SmB_6 , the first strongly correlated topological insulator, the polar surface termination provides a closely coupled ingredient in the electronic structure, with vital importance for understanding the SS required by topological bulk-boundary correspondence. Parsing ARPES spectromicroscopy data into a two-dimensional binning series enables us to separately address these coupled elements and resolve the interdependences of bulk and surface energetics over a ~ 35 meV range of chemical potentials range relative to the $4f$ bands.

Application to the Eu05 dataset reveals strongly correlated physics that can be understood from mean field theory, with doping dependence of the SS Fermi momentum and bulk $5d$ energies directly reflecting $4f$ Coulomb interactions captured by a Hubbard model. In stark contrast, we find that the greatly increased decoherence of the $4f$ state in Ce30 almost completely obscures the Hubbard model-like behavior in this sample, as the $4f$ state width becomes a dominant factor in placing the chemical potential.

Despite observing band structure with electron doped chemical potentials well outside the ~ 14 meV bulk band gap¹³, the spectral function of the X-point bulk conduction band was not apparent and remains an open question. The apparent lack of such a feature and of a clear insulator to metal transition upon doping may both be understandable if impurities cause low energy conduction band electrons are localized on an extremely short length scale. This scenario has been suggested from theoretical modeling²⁵ and closely resembles the heterogeneous valence configuration thought to underlie a much more robustly insulating phase that has been discovered in strained samples³⁹.

Observation of the highly coherent and semi-decoherent regimes of correlated physics in SmB₆ provides key insight into the unique physics of a topological Kondo system. More generally, our analysis demonstrates the use of big data from spectromicroscopy to access new observables from a single sample, including the mean field Hubbard U parameter and the interplay of chemical potential with band coherence.

References

1. Lu, F., Zhao, J. Z., Weng, H., Fang, Z. & Dai, X. Correlated Topological Insulators with Mixed Valence. *Phys. Rev. Lett.* **110**, 096401 (2013).
2. Jiang, J. et al. Observation of possible topological in-gap surface states in the Kondo insulator SmB₆ by photoemission. *Nat. Commun.* **4**, 3010 (2013).
3. Kim, D. J., Xia, J. & Fisk, Z. Topological surface state in the Kondo insulator samarium hexaboride. *Nat. Mater.* **13**, 466-470 (2014).
4. Xu, N. et al. Direct observation of the spin texture in SmB₆ as evidence of the topological Kondo insulator. *Nat. Commun.* **5**, 4566 (2014).
5. Dzero, M., Xia, J., Galitski, V. & Coleman, P. Topological Kondo insulators. *Ann. Rev. Condens. Matter Phys.* **7**, 249-280 (2016).
6. Dzero, M., Sun, K., Galitski, V. & Coleman, P. Topological Kondo insulators. *Phys. Rev. Lett.* **104**, 106408 (2010).
6. Xu, N., Ding, H. & Shi, M. Spin- and angle-resolved photoemission on the topological Kondo insulator candidate SmB₆. *J. Phys. Condens. Matter.* **28**, 363001 (2016).
7. Ohtsubo, Y. et al. Non-trivial surface states of samarium hexaboride at the (111) surface. *Nat. Commun.* **10**, 2298 (2019).
8. Eo, Y. S. et al. Transport gap in SmB₆ protected against disorder. *Proc. Natl. Acad. Sci.* **116**, 12638 (2019).
9. Li, L., Sun, K., Kurdak, C. & Allen, J. W. Emergent mystery in the Kondo insulator samarium hexaboride. *Nat. Rev. Phys.* **2**, 463-479 (2020).
10. Souza, J. C. et al. Metallic islands in the Kondo insulator SmB₆. *Phys. Rev. Res.* **2**, 043181 (2020).

11. Menth, A., Buehler, E. & Geballe, T. H. Magnetic and semiconducting properties of SmB_6 . *Phys. Rev. Lett.* **22**, 295 (1969).
12. Zhang, X. et al. Hybridization, inter-ion correlation, and surface states in the Kondo insulator SmB_6 . *Phys. Rev. X* **3**, 011011 (2013).
13. Pirie, H. et al. Imaging emergent heavy Dirac fermions of a topological Kondo insulator. *Nat. Phys.* **16**, 52-56 (2020).
14. Alexandrov, V., Dzero, M. & Coleman, P. Cubic topological Kondo insulators. *Phys. Rev. Lett.* **111**, 226403 (2013).
15. Roy, B., Sau, J. D., Dzero, M. & Galitski, V. Surface theory of a family of topological Kondo insulators. *Phys. Rev. B* **90**, 155314 (2014).
16. Denlinger, J. D. et al. Temperature dependence of linked gap and surface state evolution in the mixed valent topological insulator SmB_6 . Preprint at <http://arxiv.org/abs/1312.6637> (2013).
17. Xu, N. et al. Surface and bulk electronic structure of the strongly correlated system SmB_6 and implications for a topological Kondo insulator. *Phys. Rev. B* **88**, 121102(R) (2013).
18. Neupane, M. et al. Surface electronic structure of the topological Kondo-insulator candidate correlated electron system SmB_6 . *Nat. Commun.* **4**, 2991 (2013).
19. Kotta, E. et al. Spectromicroscopic measurement of surface and bulk band structure interplay in a disordered topological insulator. *Nat. Phys.* **16**, 285-289 (2020).
20. Xu, Y. et al. Mapping topological emergence in highly alloyed topological Kondo insulator $\text{Sm}_{1-x}\text{M}_x\text{B}_6$ ($\text{M}=\text{Eu}, \text{Ce}$). *Phys. Rev. B* **104**, 115118 (2021).
21. Miao, L. et al. Robust surface states and coherence phenomena in magnetically alloyed SmB_6 . *Phys. Rev. Lett.* **126**, 136401 (2021).
22. Zhu, Z.-H. et al. Polarity-driven surface metallicity in SmB_6 . *Phys. Rev. Lett.* **111**, 216402 (2013).
23. Denlinger, J.D. et al. SmB_6 Photoemission: Past and Present. Preprint at <http://arXiv.org/abs/1312.6636> (2013).
24. Alexandrov, V., Coleman, P. & Erten, O. Kondo breakdown in topological Kondo insulators. *Phys. Rev. Lett.* **114**, 177202 (2015).
25. Skinner, B. Properties of the donor impurity band in mixed valence insulators. *Phys. Rev. Materials* **3**, 104601 (2019).

26. Thunström, P. & Held, K. Topology of SmB₆ determined by dynamical mean field theory. *Phys. Rev. B* **104**, 075131 (2021).
27. Phelan, W. et al. On the chemistry and physical properties of flux and floating zone grown SmB₆ single crystals. *Sci. Rep.* **6**, 20860 (2016).
28. Kang, B. Y. et al. Magnetic and nonmagnetic doping dependence of the conducting surface states in SmB₆. *Phys. Rev. B* **94**, 165102 (2016).
29. Yeo, S., Song, K., Hur, N., Fisk, Z. & Schlottmann, P. Effects of Eu doping on SmB₆ single crystals. *Phys. Rev. B* **85**, 115125 (2012).
30. Gabáni, S. et al. Transport properties of variously doped SmB₆. *Phil. Mag.* **96**, 3274-3283 (2016).
31. He, H. et al. Irreversible proliferation of magnetic moments at cleaved surfaces of the topological Kondo insulator SmB₆. *Phys. Rev. B* **95**, 195126 (2017).
32. Lutz, P. et al. Valence characterization of the subsurface region in SmB₆. *Phil. Mag.* **96**, 3307-3321 (2016).
33. Rößler, S. et al. Surface and electronic structure of SmB₆ through scanning tunneling microscopy. *Phil. Mag.* **96**, 3262-3273 (2016).
34. Sun, Z. et al. Observation of a well-defined hybridization gap and in-gap states on the SmB₆ (001) surface. *Phys. Rev. B* **97**, 235107 (2018).
35. Crivillero, M. et al. Phase stability in SmB₆. *Phys. Rev. Mat.* **5**, 044204 (2021).
36. Yee, M. et al. Imaging the Kondo insulating gap on SmB₆. Preprint at <https://arxiv.org/abs/1308.1085> (2013).
37. Valentine, M. et al. Breakdown of the Kondo insulating state in SmB₆ by introducing Sm vacancies. *Phys. Rev. B* **94**, 075102 (2016).
38. Matt, C. E. et al. Consistency between ARPES and STM measurements on SmB₆. *Phys. Rev. B* **101**, 085142 (2020).
39. Stern, A. et al. Surface-dominated conduction up to 240 K in the Kondo insulator SmB₆ under strain. *Nature Materials* **16**, 708-711 (2017).
40. Open source software developed for this manuscript can be found at https://github.com/eck-nyu/SmB6_XYmap_analysis

41. Min, C.-H. et al. Matching DMFT calculations with photoemission spectra of heavy fermion insulators: universal properties of the near-gap spectra of SmB₆. *Sci. Rep.* **7**, 11980 (2017).
42. Liu, S. et al. Fourier-based methods for removing mesh anomalies from angle resolved photoemission spectra. Preprint at <https://arxiv.org/abs/2112.11516>.

Figures

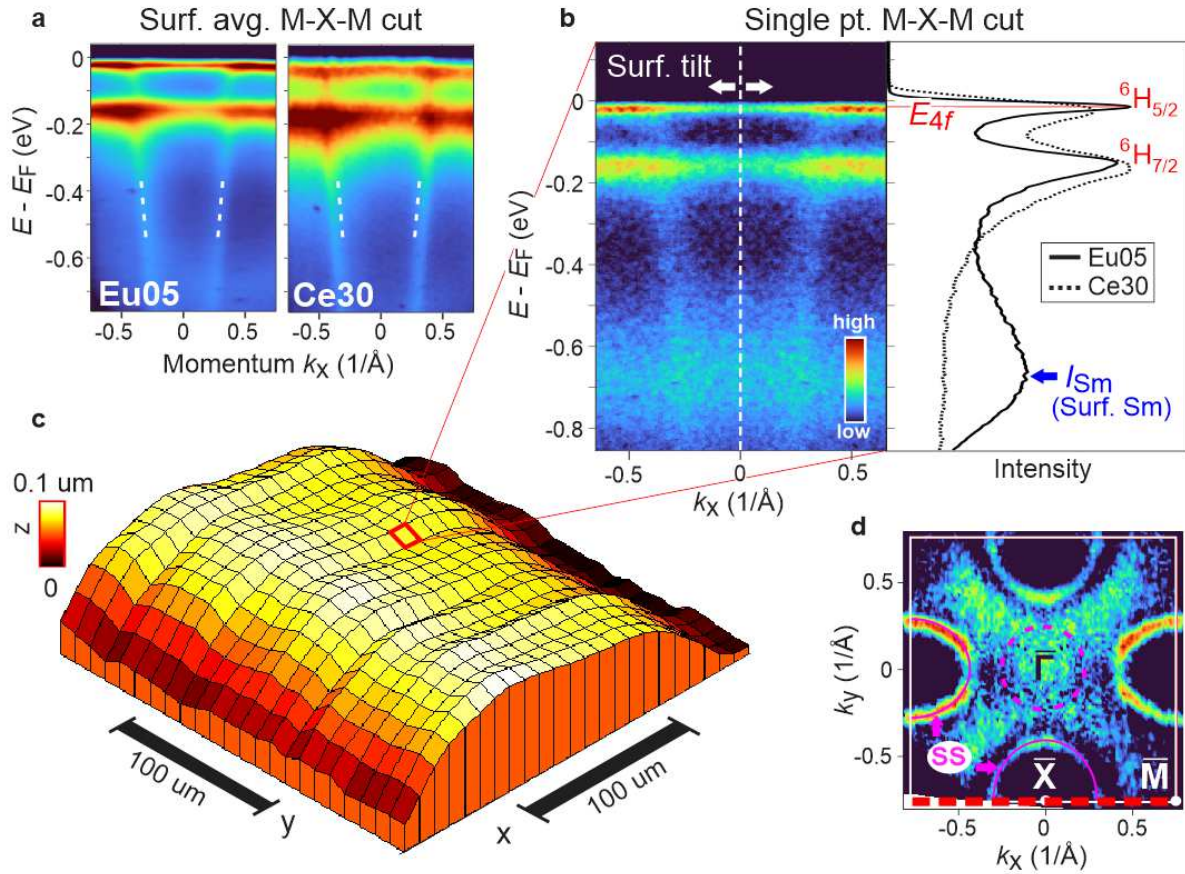


Figure 1: Mapping an SmB_6 surface with micro-ARPES. **a**, ARPES scans of Eu05 and Ce30, spatially averaged across the entire sample surface. A segment of the Eu05 $5d$ band dispersion is traced on both panels. **b**, A symmetrized single-point ARPES scan of Eu05. Surface tilt is determined from the position of the $k_x=0$ symmetry axis (dashed white line) on the ARPES detector. A k -integrated profile at right contrasts Eu05 with a typical Ce30 surface spot, and is labeled with the $4f$ band symmetries and an $E=-0.7$ eV Sm^{2+} multiplet feature used to identify excess surface Sm (I_{Sm}). **c**, An approximate height profile of the Eu05 surface, reconstructed from the surface tilt data. **d**, A Fermi surface scan of Eu05 is labeled with a red dashed line indicating the $\bar{M}-\bar{X}-\bar{M}$ axis used for ARPES measurements (roughly M-X-M in the bulk Brillouin zone). Topological SS surrounding the \bar{X} -point are traced in magenta. Additional SS near the Brillouin zone center are not visible in this experimental configuration.

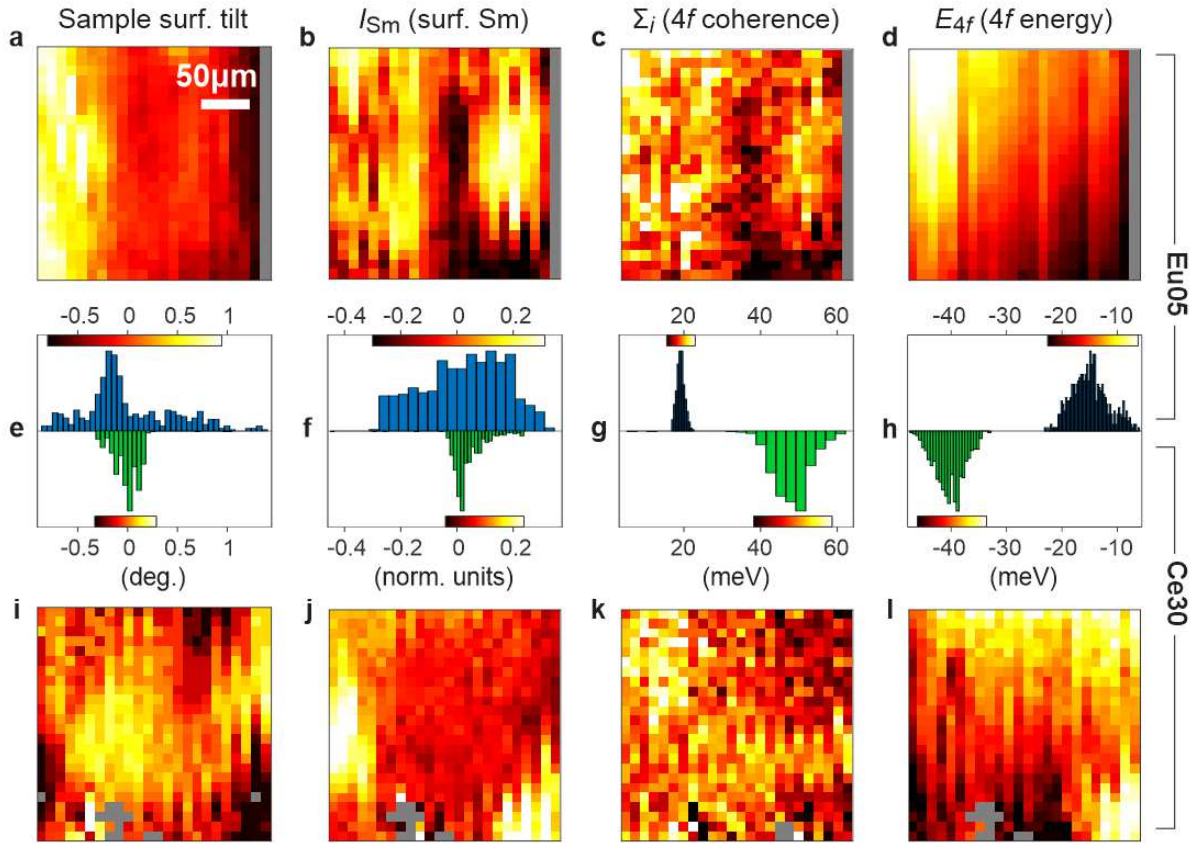


Figure 2: Electronic structure surface maps. **a-d**, Maps of the surface tilt, surface Sm density (I_{Sm}), $4f$ feature width (Σ_i), and $4f$ energy (E_{4f}), respectively, catalogued over the Eu05 sample surface. Excluded data are marked in gray (see Methods). **e-h**, Histograms comparing the distributions of the four spectral features for (top) Eu05 and (bottom) Ce30. Histogram bin widths are set to the standard fitting error, and color bars show the dynamic range in each corresponding surface map. **i-l**, Surface maps of the same spectral feature properties for the Ce30 sample.

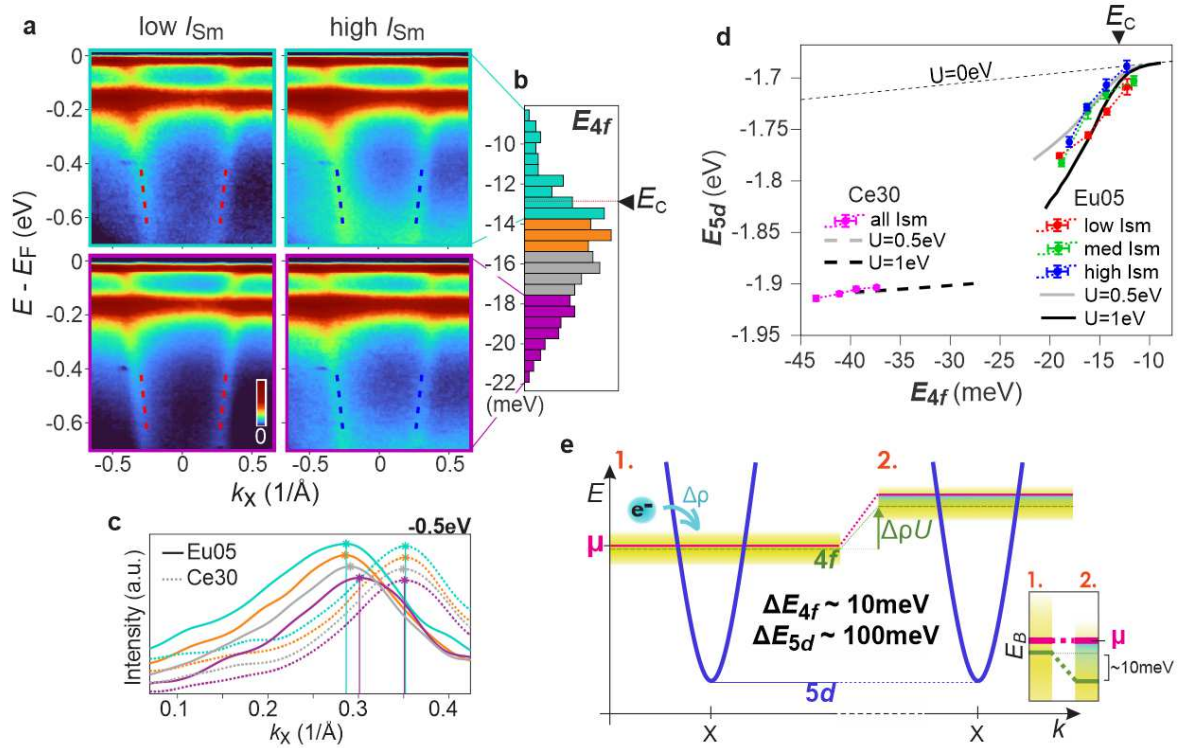


Figure 3: Strong correlations in the bulk electronic structure. **a**, Binned spectral images show differences between the top and bottom quartiles for 4f band energy (E_{4f}) and surface Sm density (I_{Sm}). Bulk 5d dispersions traced on the (top) high E_{4f} panels are reproduced in the bottom panels, revealing a ~ 0.1 eV shift in the 5d band energies. **b**, Binned regions are shaded on a histogram of 4f band energy (E_{4f}). **c**, Momentum distribution curves at $E = -0.5$ eV showing variable size of the 5d electron pocket for E_{4f} quartile bins. Curves are vertically offset, with lowest- E_{4f} (highest chemical potential) at the bottom. **d**, The 5d band energy (E_{5d}) is shown as a function of E_{4f} for Eu05 and Ce30. **e**, Illustration of the role of strong correlations in a mean field picture. When doped electrons change the 4f charge density by $\Delta\rho$, the 4f band energy increases by $\Delta\rho U$ (picture at right). The chemical potential μ shifts in tandem with the 4f states, with the net effect that the 5d bands (E_{5d}) move down in energy relative to E_{4f} and the Fermi level.

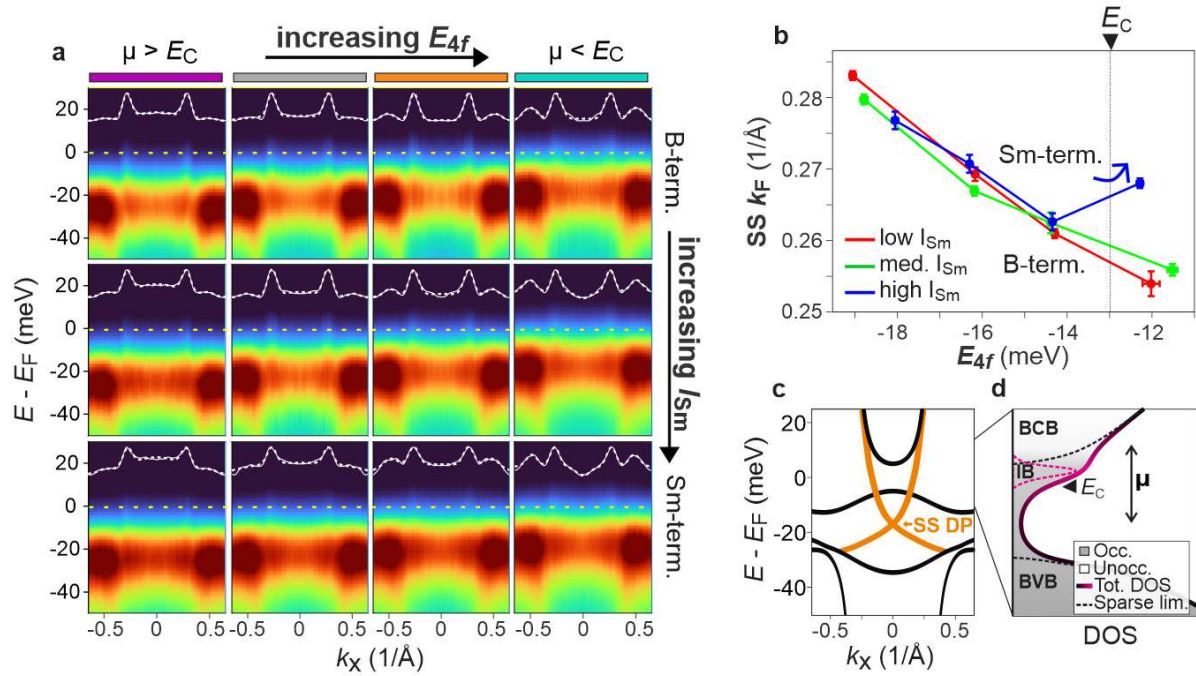


Figure 4: Chemical potential and the topological surface state. **a**, Binned spectral images show SS evolution as a function of charge doping (E_{4f}) along rows and surface Sm density (I_{Sm}) along columns. Each image includes a Fermi level momentum distribution curve and overlaid Gaussian fit. **b**, The SS Fermi momentum is shown as a function of $4f$ energy (E_{4f}), from the fits in panel (a). **c**, The approximate range of the Eu05 chemical potential (μ) is shown with respect to a tight binding model of (black) the M-X-M bulk states and (orange) the SS dispersion. **d**, An illustration of likely features in the DOS distribution, including the bulk conduction band (BCB), valence band (BVB), and a continuum of bound or localized states (IB).

Methods

Single crystals of $\text{Sm}_{0.95}\text{Eu}_{0.05}\text{B}_6$ (Eu05) and $\text{Sm}_{0.7}\text{Ce}_{0.3}\text{B}_6$ (Ce30) were prepared by the alumina flux method, described in Ref. [21,27]. Characterization of these compositions can be found in Ref. [20-21,28-30], and has shown single phase growth with lattice parameters that evolve monotonically with the Eu and Ce alloy fraction. Measurements in Ref. [21] address dopant homogeneity, impurity multiplet states, surface stability, and the 2D nature of attributed SS.

ARPES measurements were performed at the ESM beamline at NSLS-II, with a base pressure better than 5×10^{-11} Torr. Samples were cleaved *in situ* at $T=10\text{K}$ and measurements taken within 10 hours of cleaving. Photon energy was set to $h\nu=70$ eV corresponding to a bulk Γ -plane ($k_z=0$) of the cubic Brillouin zone. The energy resolution was $\delta E \sim 10$ meV, and momentum resolution was $\delta k < 3 \times 10^{-3} \text{ \AA}^{-1}$. Analysis software developed for the project can be accessed via the link in Ref. [40].

Previously characterized inhomogeneity in SmB_6 samples

Our measurements reveal a large dynamic range in electronic structure surveyed on the micron scale across the surface of single flux-grown Eu05 and Ce30 samples. The origin of this variability is necessarily linked to nanostructure observed in numerous STM studies on SmB_6 , which have shown inhomogeneities in various properties including local stoichiometry, surface termination, and surface reconstruction³³⁻³⁶, with Sm vacancies typically implicated as the most common point defects. A recent characterization of non-stoichiometrically flux-grown Sm_xB_6 ($x=0.9, 0.75, 0.6$) found 1-3% Sm deficiency, with the most nearly stoichiometric growth achieved at $x=0.75$ ³⁵. Flux growth makes use of relatively low growth temperatures, which can reduce defect density, but the samples are nonetheless susceptible to flux inclusions, contamination from the melt container, and possible inhomogeneities associated with different facets that develop during growth²⁷. The amount of aluminum flux retained within samples also varies significantly, with the same flux growth method noted to yield a range from ~ 0 -4% Al by weight²⁷. Little is known about the degree of homogeneity *within single samples*, though cross sections along rod-like floating zone samples have noted stoichiometry gradients with attributed differences at the $\sim 1\%$ level^{27,37}.

The low temperature placement of the chemical potential is difficult to predict from these factors, particularly given the large $4f$ feature width (Σ_i) observed in our samples. Theoretical modeling places a very large DOS maximum just beneath the insulating band gap, and any effect that broadens this DOS peak will cause the chemical potential to be driven upward, as is necessary to preserve electron number. This repulsion of the chemical potential has a strong short-range component, making it challenging to dope towards the valence band. Correlated DMFT modeling places a much smaller DOS maximum associated with the 7F_3 multiplet state roughly 60 meV above the band gap^{16,26,41}, which is likely responsible for stabilizing the chemical potential within the observed $<\sim 30$ meV window above the Kondo gap.

Comparison of Eu05 and undoped SmB₆

The Eu05 composition was favored over undoped SmB₆ for this investigation, primarily because the surface Sm²⁺ multiplet feature that defines I_{Sm} is far weaker in surface surveys of Eu05 (see Fig. S1, right panels). This multiplet feature overlaps with the $5d$ bands and can potentially distort their apparent dispersion through hybridization. This problematic background can be seen in the error bars of the high- I_{Sm} Eu05 curve of Fig. 4a, which are roughly 70% larger than the low- I_{Sm} curve. The mean I_{Sm} value observed for the undoped compound is 0.24, compared to 0.02 for the Eu05 data, and renders investigation of the $5d$ band energy (E_{5d}) much more challenging. Based on STM surface surveys²¹, we speculate that inhomogeneity from alloying contributes to the appearance of rough surfaces that lack a cleanly defined Sm- or B- termination.

A further advantage of Eu05 is that it shows a range of chemical potentials that is roughly 1.3x as broad as in undoped SmB₆ (see Fig. S1, left panels). A primary difference is that the compound shows almost no surface locations with in-gap chemical potentials ($E_{4f} > E_C$). This matches expectations based on the interpretation of the E_{4f} histogram as approximately representing the electronic density of states distribution multiplied onto an intensity contour derived from the range of local structural/chemical environments (see main text discussion). The smaller E_{4f} distribution and apparent lack of in-gap impurity states are both in keeping with the undoped compound having relatively few impurities. The observation of in-gap chemical potentials in Eu05 may also be in keeping with the expectation that Eu_{Sm} substitution sites will act as effective hole dopants.

Feature tracking procedures

The four spectral features identified in an individual ARPES image (Fig. 1b) were quantified by the following procedures⁴⁰. Due to the specific metrics of interest and to superior single-image statistics relative to Ref. [19], band fitting was preferred over template matching.

1. **Surface tilt angle**: Constant energy data curves were analyzed at energies $E-E_F = -0.3$ to -0.6 eV in 10-meV intervals. The angle coordinates of the peaks associated with the left and right branches of the $5d$ -band were fitted for each energy, and the mean of all values was set as the surface normal angle.
2. **4f band energy E_{4f}** : The surface tilt angle map from (1) above was used to identify precise momentum coordinates for each image. ARPES intensity in each image was then summed over a large range of k values $[-0.55, 0.55] \text{ \AA}^{-1}$. The $4f$ energy E_{4f} is set to the energy of the highest-energy peak, associated with the $4f$ states immediately beneath the Fermi level ($J=5/2$ symmetry). A much broader peak at $E-E_F \sim -0.15$ eV derives from the $4fJ=7/2$ states and was tracked using the same method. The $J=7/2$ state can be used as a sanity check for E_{4f} , and produces a qualitatively identical map and derivative analysis when used in lieu of the $J=5/2$ state (see Extended Data Fig. S2).
3. **4f energy width Σ_i** : The energy width of the $4f$ band is defined as the full width at x maximum of the intensity peak from step 2, with x set to 0.75 to reduce the effect of overlap with the neighboring $J=7/2$ feature. Dependence on the x value is explored in Extended Data Fig. S3, and does not qualitatively change the surface map.
4. **Surface Sm density I_{Sm}** : Momentum/energy windows were selected to represent A) a region on top of the broad and flat Sm^{2+} multiplet feature seen near -0.7 eV in Fig. 1b, and B) a background region near -0.4 eV, with both regions chosen to avoid intensity from the $5d/4f$ bands. I_{Sm} is defined with respect to the mean intensity in these windows (I_A and I_B), as $I_{Sm} = (I_A - I_B)/I_B$.

Reconstructing a sample height profile

Tilt map values represent the angle between the surface normal and the center of the ARPES analyzer slit, which is parallel to the sample x axis in the experimental geometry. Height differences between a given point and its neighbor along the sample x axis can be approximated by $\Delta x \times \tan(\theta)$, with Δx being the step size along x (10 μm) and θ the tilt angle at that point. Integrating over all x coordinates, and arbitrarily setting the height of the first point to 0, a height profile along x can be created at each y coordinate. The height profile of the Eu05 sample surface in Fig. 1c represents the average of two methods illustrated in Extended Data Fig. S3: 1. Setting the left-most column height to 0 and integrating $\Delta x \times \tan(\theta)$ to the right, and 2. Setting the right-most column height to 0 and integrating $-\Delta x \times \tan(\theta)$ to the left.

This approach cannot accurately reproduce feature variation along the y-axis, but is nonetheless useful for visualizing the approximate height profile and range of tilt variation. Large y-axis tilt results in deviation of the ARPES cut from the $\overline{M-X-M}$ axis ($k_y = -\pi/a$), with potential consequences for estimates of 5d band binding energy E_{5d} . However, the metrics assessed in this paper are relatively insensitive to this variation, as assessed in the error analysis section below.

Identifying the 5d band minimum E_{5d}

The energy difference from point to point in a given curve within Fig. 3d was evaluated by taking the difference in the mean 5d band momenta at -0.45 eV, and multiplying by the band velocity. Velocity of the 5d band was set to the average value of $v_{5d, \text{Eu05}} = 3.6 \text{ eV-}\text{\AA}$ for Eu05, and $v_{5d, \text{Ce30}} = 4.2 \text{ eV-}\text{\AA}$ for Ce30. Based on the tight binding model 5d dispersion, the use of an average value rather than a curve-dependent value is expected to create negligible (<2%) error in all single curve point-to-point energy differences.

The average 5d band minimum was set to 1.7 eV for the shallowest binding energy Eu05 data points, in keeping with estimates from the undoped sample, and the energy difference between the Ce30 and Eu05 curves was identified using the average of the Ce30 and Eu05 v_{5d} values. Though E_{5d} is framed as the band minimum, we note that it is fitted from roughly the center of the band dispersion, and the physical quantity it primarily corresponds to is the mean energy of the 5d orbital (the orbital energy in a tight binding model).

Evaluating surface state velocity

The SS velocity discussed in the text surrounding Fig. 4 is determined from a series of momentum distribution curves (MDC) taken near the Fermi level, by tracking the shift of the intensity peaks throughout a 6 meV range immediately beneath the Fermi level (see Extended Data Fig. S5). This gives a velocity $v_{F,SS} \sim 0.50 \text{ eV}\text{\AA}$.

Error analysis

Error in the measured feature maps of Figure 2 is estimated by evaluating the variance from pairs of neighboring points, under the approximation that the slope along the vertical (y-) axis will be negligible. This approximation necessarily leads to a slight overestimation of error bars. In the procedure, N pairs of beam spot coordinates are sampled from a map, with the two coordinates in a pair lying vertically adjacent along the sample y-axis. A rough upper bound on the standard error is then estimated by

$$\sigma = \sqrt{\frac{1}{N} \sum_{i=1}^N S_i^2} \quad (1)$$

for sufficiently high N , where S_i^2 is the variance of the i^{th} pixel pair defined as $S^2 = \Sigma(b - \bar{b})^2$. Here b is a vector of the two map feature values (of the i^{th} pixel pair), and \bar{b} the average value.

Error from tilt

Maximal tilt error for the Eu05 sample may be as large as $\sim 1^\circ$ based on the tilt range in Fig. 2a, corresponding to a shift of $\Delta k = 0.07 \text{ \AA}^{-1}$ in momentum space. Only shifts along the Γ -X momentum axis will contribute to systematic error, and the reconstructed height profile suggests that error along this direction is relatively small (see Fig. S4 of Extended Data and next section discussion). The most sensitive feature to this tilt error is the $5d$ band radius, which is expected to be roughly 0.3 \AA^{-1} along the X-M axis and slightly larger along Γ -X in the binding energy range of interest. Factoring in the X-M band velocity of $v = 3.6 \text{ eV}\text{-}\text{\AA}$, the potential reduction in apparent X-M axis band momentum as a result of surface-tilt-induced Γ -X momentum displacement yields a maximal energy shift of $\sim < 0.02 \text{ eV}$ in the E_{5d} value within single-point

ARPES images from the sample surface. Based on the Fig. 1e height profile reconstruction, we expect the overall effect on the Fig. 3d curves to be reduced to <0.01 eV as points are obtained from binning over the surface.

Mechanical hysteresis

The spatial scans were performed column-wise, starting from the left-most sample x position and advancing from top to bottom along the sample y axis at each x coordinate. Applying an x-dependent offset to the sample y position values, $y_0(x)$, can reduce the appearance of the vertical stripe-like features seen throughout the Figure 2 maps, possibly showing a truer representation of the underlying spatial structure. Figure S6 of the extended data shows an example of corrections applied to all Eu05 maps ($y_{0,\text{Eu05}}$) and Ce30 maps ($y_{0,\text{Ce30}}$), with correction offsets determined by eye to minimize the appearance of the strip-like features.

Sampling Bias

The single-point standard error in E_{4f} values is less than 1 meV for both Eu05 and Ce30 datasets, and is determined to account for a $\sim 1\%$ reduction in the total range of bin-resolved E_{4f} values in Fig. 3d. To evaluate this, the distribution is first deconvoluted by the fitting error to approximate the true underlying E_{4f} distribution. This distribution is then re-convoluted with the fitting error to identify the ‘true’ mean E_{4f} value in each bin of the binning series, as described in the Supplemental Information of Ref [19].

Sampling bias along the I_{Sm} axis is also important to consider, particularly for data points with $E_{4f} > E_C$ at the extreme hole-doped side of Fig. 3d and 4b. High I_{Sm} values correlate with relative hole doping in the bulk bands (more positive E_{4f}), and this means that the data points at the hole and electron doped ends of the E_{4f} distribution come from binned data with relatively high and low mean I_{Sm} values, respectively. This issue can be neglected at the electron-doped end of the distribution, where the high- and low- I_{Sm} sections show a similar linear trend that does not change upon rebinning with a greater number of I_{Sm} subdivisions (data not shown).

Sample Aging

All measurements were performed within 10 hours of cleavage, a time scale that largely precludes aging effects in the low energy spectrum for samples maintained at $T \sim 10\text{K}$ [21]. Nonetheless, aging during the measurement may result in some weakening of the surface Sm multiplet feature (I_{Sm}). Such an effect appears to be visible as a left-to-right gradient in the Fig. 2j Ce30 I_{Sm} map, due to the small dynamic range of the color scale. We note that the gradients in the E_{4f} maps do not appear to be associated with aging, as they align with the diagonal of the image rather than with the left-to-right time-axis of the measurement, and the sign of the time-axis gradient in Eu05 is opposite to expectations based on the oxidative trend of surface aging³¹⁻³².

Excluded Data and Analysis

Gray pixels throughout the Fig. 2 feature maps represent “bad” data, for which one or more features could not successfully be evaluated (or data was not taken, as for the last column of pixels in the Eu05 spatial scan). Failure of fitting algorithms is most commonly due to low signal-to-noise or signal-to-background, possibly resulting from structural irregularities that could not be spatially resolved.

SS Fermi momentum analysis is omitted for the Ce30 data due to limited resolution of the SS band in this sample. Not only is the SS feature broader in Ce30 and thus more difficult to track, but the background it sits upon is dramatically increased by the large $4f$ state width noted in Fig. 2g. These factors combine with minor modulations of this background from incomplete removal of the ARPES mesh pattern⁴² to yield error that is unacceptable for a close analysis.

Tight binding+U calculations

The SmB_6 tight binding model was based on the implementation in Ref. [25], which considers a Sm-only basis of six $J=5/2$ $4f$ states and two $5d$ e_g orbitals per unit cell. Parameters of the model are identical to Ref. [20], in which the $5d$ dispersion is aligned to experimental data on the Γ -X axis, and the $4f$ renormalization and crystal field energetics are tuned based on dispersion and symmetry features noted in recent literature.

Mean field calculations for Eu05

For the Eu05 sample, we assume that variation in the chemical potential stems directly from carrier doping. The on-diagonal energy of 4*f* orbitals (ϵ_f) was modified to the mean field value of:

$$\epsilon_f'(U, n) = \epsilon_f + U \times [n_f(U, n) - n_f(0, 6)] \quad (2)$$

where U is the on-site 4*f*-4*f* Coulomb interaction parameter (Hubbard U), n is the number of electrons per Sm atom ($n=6$ for an undoped sample), and $n_f(U, n)$ is the expectation value of 4*f* electron number for given values of U and n . The value of $n_f(U, n)$ and associated estimate of $\epsilon_f'(U, n)$ were iteratively converged through repeated diagonalizations of the tight binding Hamiltonian over a dense mesh covering the Brillouin zone.

Impact of strong correlations on the surface state Fermi momentum

In the tight binding model, the SS Fermi momentum shifts at a rate of $0.148 \text{ \AA}^{-1}/\text{eV}$ as one reduces the 5*d* band energy E_{5d} . This rate can be used to evaluate the effect of strong correlations on the SS Fermi momentum, when combined with the empirically observed value of $m_{df} \sim 15$ in the linear region of the doping series.

In a rigid shift picture, the expected k -shift of the SS Fermi momentum within the linear region of Fig. 4b, where the 4*f* state shifts by $\Delta E_{4f} = 5 \text{ meV}$, is $\Delta k_{F,SS} = 0.010 \text{ \AA}^{-1}$ ($=0.005 \text{ eV} / 0.50 \text{ eV-}\text{\AA}$). This differs by nearly a factor of 2 from the observed $k_{F,SS}$ shift of $\Delta k_{F,SS} = 0.019 \text{ \AA}^{-1}$ ($=0.005 \text{ eV} / 0.26 \text{ eV-}\text{\AA}$). Factoring in the corresponding 75 meV binding energy shift of the 5*d*-band from strong correlations ($75 \text{ meV} = \Delta E_{4f} \times m_{df}$), we find that correlations yield an additional Fermi momentum shift of $0.010 \text{ \AA}^{-1} = (0.075 - 0.005 \text{ meV}) \times 0.148 \text{ \AA}^{-1}/\text{eV}$. This is an excellent match for the 0.009 \AA^{-1} discrepancy ($0.010 \text{ \AA}^{-1} = 0.019 \text{ \AA}^{-1} - 0.010 \text{ \AA}^{-1}$), given the intrinsic uncertainty in the modeling.

Mean field calculations for Ce30

A self-consistency condition was used to calculate the Ce30 band structure. The dependence of 4*f* binding energy (E_{4f}) on 4*f* self energy (Σ_i) has been established from temperature-dependent studies on SmB₆¹⁶. However, given $E_{4f}(T)$ and $\Sigma_i(T)$, we obtain an incorrect charge density $n(T)$;

to correct for this, we add in a correction that is assumed to come from above the Fermi level (from multiplet features captured in DMFT, but not in the tight binding model), and iteratively converge the electronic structure with the nominal Hubbard U value.

The size of the $4f$ energy shift is large relative to the attributed variation of Σ_i across our Ce30 sample, and resembles the much larger shift that would be expected in a bare tight binding model, without DOS compensation from above the Fermi level. Some electron count is expected to come from the $4f J=7/2$ DOS peaks, but this contribution is lost when the convolution becomes Gaussian (disorder) instead of Lorentzian (imaginary self energy).

While this trend matches expectations, it is puzzling that one does not see evidence for inhomogeneity in the dopant density, in contrast to the case for Eu05. This may be explained by a number of factors, one coming from the fact that the doping contribution m_{df} is linearly proportional to the $\text{DOS}_{4f}/\text{DOS}_{5d}$ ratio. Less coherent $4f$ states have smaller associated DOS peaks, and the $4f$ state fraction will also decline as one raises the chemical potential further into the conduction band; these contribute to significantly reduced doping effects. A new $5d$ electron pocket is also expected to intersect the Fermi level (along the Γ -M axis) at roughly the binding energy seen in this sample, additionally contributing to higher $5d$ -DOS and thus reduced doping contribution.

The physical structure of the sample may also be significant. The variation in chemical potential comes from sample growth dynamics and not from root- N statistical fluctuations, which are tiny. As such a trivial explanation may be that the impurity distribution in the Ce30 sample is simply more uniform than in Eu05, consistent with the flatter and more homogeneous surface seen in our Fig. 2c maps of tilt angle and termination chemistry. Taken together, these factors provide a scenario in which the doping dependence may no longer be resolved.

Data availability

All relevant data are available from the corresponding authors upon reasonable request.

Code availability

All relevant source code or algorithms are available online⁴⁰ or from the corresponding authors upon reasonable request.

Acknowledgements

This research used the ESM beamline at the National Synchrotron Light Source II, a U.S. Department of Energy (DOE) Office of Science User Facility operated for the DOE Office of Science by Brookhaven National Laboratory under Contract No. DE-SC0012704. This research used resources of the Advanced Light Source, a U.S. DOE Office of Science User Facility under Contract No. DE-AC02-05CH11231. L.A.W. acknowledges the support of the National Science Foundation under grant No. DMR-2105081. J.W.L., and B.K.C. were supported by the National Research Foundation of Korea (NRF), funded by the Ministry of Science, ICT and Future Planning (No. NRF2017R1A2B2008538). L.M. is supported by the National Natural Science Foundation of China (Grants No. U2032156 and No. 12004071) and Natural Science Foundation of Jiangsu Province, China (Grant No. BK20200348).

Author Contributions

T.Y., E.K., Y.X., and L.M. carried out the ARPES experiments, with support from J.D.D. and E.V.; high quality samples were synthesized and characterized by J.W.L. with guidance from B.K.C.; computational data analysis and tight binding simulations were implemented by E.K. and Y.X., Yi X., and D.J., with assistance from L.A.W.; E.K., Y.X., J.W.L., B.K.C. and L.A.W. participated in the analysis, figure planning and draft preparation; L.A.W. was responsible for the conception and the overall direction, planning and integration among different research units.

Competing interests

The authors declare no competing financial or non-financial interests.

Extended Data & Figures

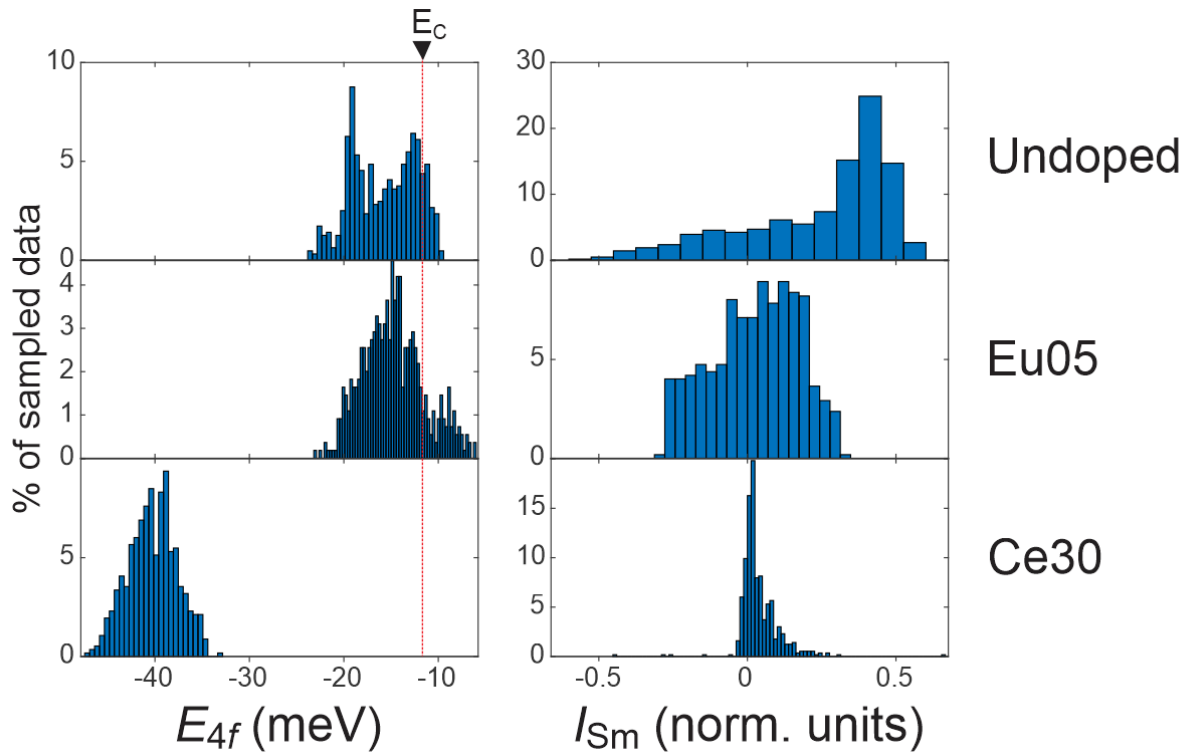


Figure S1: Chemical potential and surface termination. (left column) Histograms of the 4f state energy relative to the Fermi level E_{4f} for undoped, Eu05 and Ce30 samples. (right column) Intensity of the samarium termination multiplet feature (I_{Sm}) for each sample. Histogram bin width is set to the standard fitting error. The Fermi energy of each sample was identified via momentum-axis fitting, which showed a step function-like amplitude loss at the Fermi level.

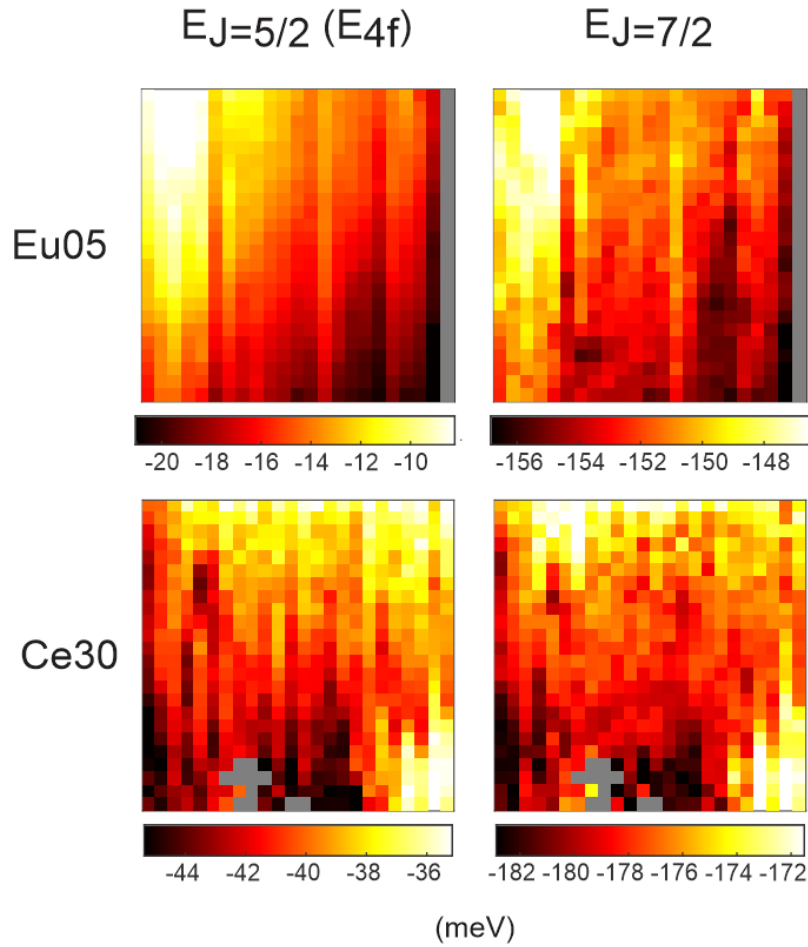


Figure S2: Comparison of the $J=5/2$ and $J=7/2$ energies. (left column) The $J=5/2$ $4f$ state is used to determine $4f$ state energy E_{4f} throughout the text. (right column) The $J=7/2$ state is fixed roughly ~ 130 meV lower in energy, and may in principle be used for the same purpose. All derivative analyses of Figs. 3-4 using the $J=7/2$ state distribution in place of the $J=5/2$ state reproduce qualitatively identical results.

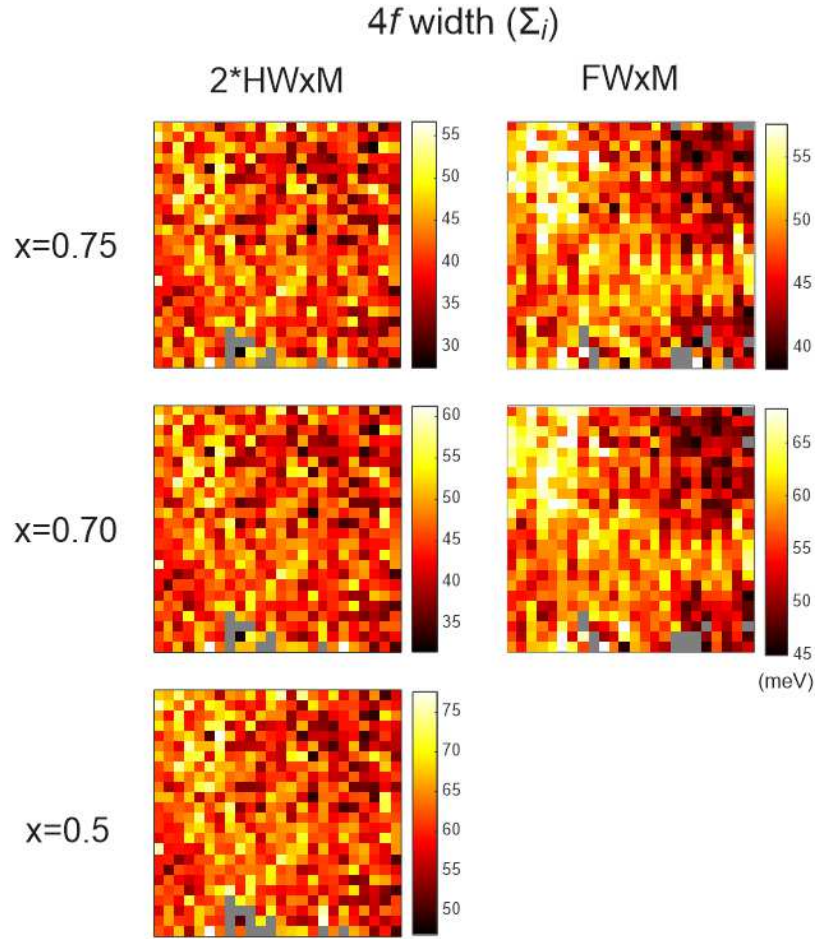


Figure S3: Ce30 $4f$ energy width (Σ_i) maps at x -maximum. (left column) The energy width Σ_i of the $J=5/2$ $4f$ feature at the fraction x of peak height is evaluated as twice the half-width on the side of the feature that is closest to the Fermi level. (right column) Energy width is evaluated as full width of the feature, yielding superior statistics. The $x=0.75$ full width map used in Fig. 2 shows the same features as the $x=0.5$ half width map, with roughly $<10\%$ greater amplitude.

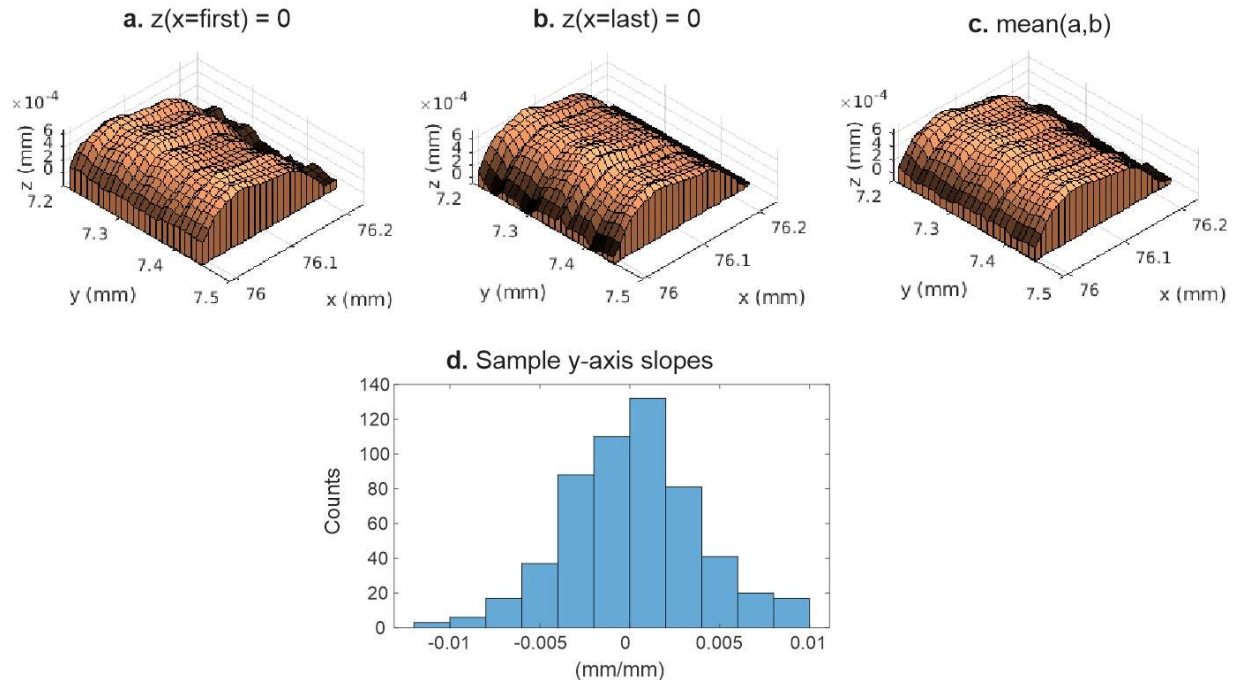


Figure S4: Reconstructing the height profile from surface tilt. **a**, The surface profile is obtained by setting height to 0 for the first column of values (minimum x), then integrating $+\Delta x \times \tan(\text{tilt}(x))$ to for each y row. **b**, The starting point height is set to 0 for the last column of values (maximum x) and height profile created by integrating $-\Delta x \times \tan(\text{tilt}(x))$ to the left (decreasing x). **c**, The final height profile (Fig. 1c) is taken as the average of the two previous methods. **d**, Histogram of y -axis slope evaluated from nearest neighbor height values across the sample surface.

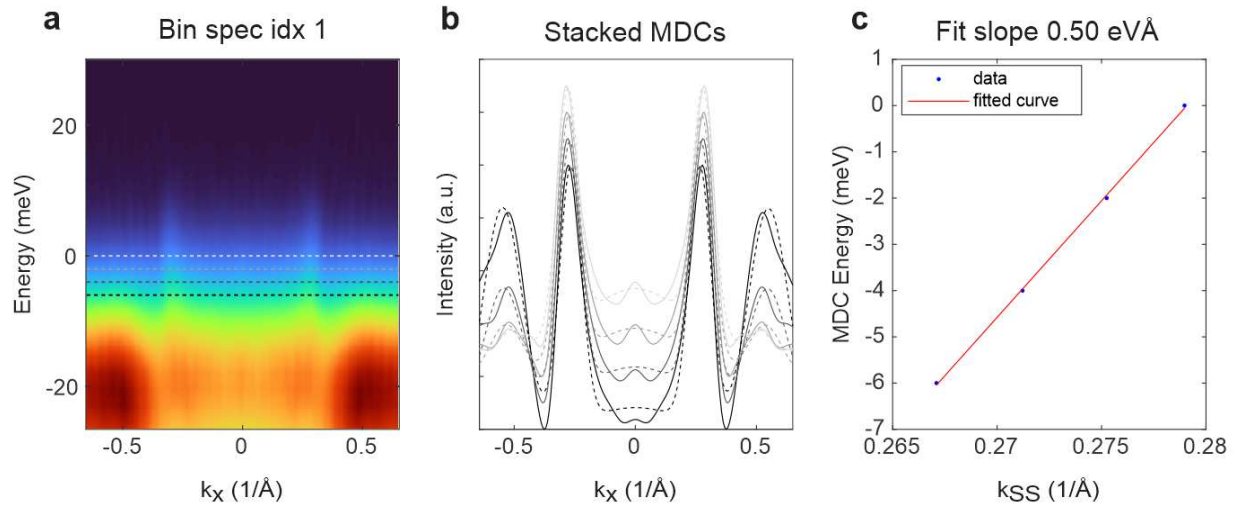


Figure S5: Determining surface state velocity. **a**, MDCs are taken at 2-meV intervals between -6 meV to 0 meV, from the binned spectrum at the top-left of Fig. 3b. **b**, The SS momentum $k_{SS}(E)$ is approximated for each energy by Gaussian peak fitting of the MDC. **c**, Summary of k_{SS} versus energy. The SS velocity fitted from all 4 points is $v=0.50$ eV-Å⁻¹, and pairwise point-to-point estimates are all >96% of this value.

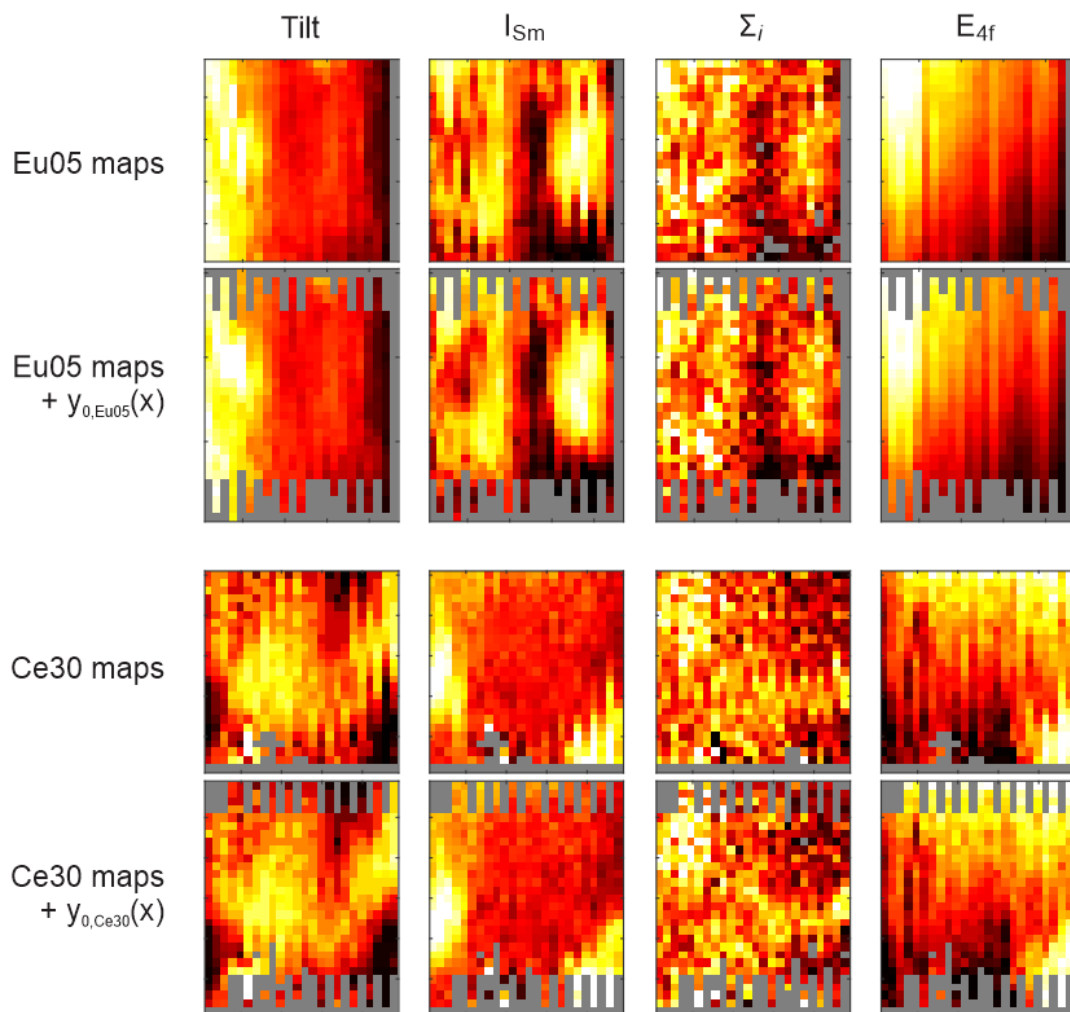


Figure S6: Correcting stripe artifacts in feature maps. Correcting mechanical hysteresis with an x -dependent offset to the sample y -axis $y_0(x)$. Specific forms of $y_0(x)$ are estimated by eye to reduce the vertical stripe-like features.